

Relativistic Iron Emission and Disk Reflection in Galactic Microquasar XTE J1748–288

J. M. Miller,¹ D. W. Fox,¹ T. DiMatteo,^{2,5} R. Wijnands,^{1,5} T. Belloni,³ D. Pooley,¹ C. Kouveliotou,⁴ W. H. G. Lewin¹

Subject headings: Black hole physics – line:profiles – relativity – X-rays:bursts

ABSTRACT

We report evidence for an Fe K α fluorescence line feature and disk reflection in the Very High, High, and Low State X-ray spectra of the galactic microquasar XTE J1748–288 during its June 1998 outburst. Spectral analyses are made on data gathered throughout the outburst by the *Rossi X-ray Timing Explorer* Proportional Counter Array. Gaussian line, relativistic disk emission line, and ionized disk reflection models are fit to the data. In the Very High State the line profile appears strongly redshifted, consistent with disk emission from the innermost stable orbits around a maximally rotating Kerr black hole. In the High State the line profile is less redshifted and increasingly prominent. The Low State line profile is very strong (\sim 0.5 keV equivalent width) and centered at 6.7 ± 0.10 keV; disk line emission model fits indicate that the inner edge of the disk fluctuates between \sim 20 and \sim 100 R_g in this state. The disk reflection fraction is traced through the outburst; reflection from an ionized disk is preferred in the VHS and HS, and reflection from a relatively neutral disk is preferred in the LS. We discuss the implications of our findings for the binary system dynamics and accretion flow geometry in XTE J1748–288.

¹Center for Space Research and Department of Physics, Massachusetts Institute of Technology, Cambridge, MA 02139–4307; jmm@space.mit.edu, derekfox@space.mit.edu, rudy@space.mit.edu, davep@space.mit.edu, lewin@space.mit.edu

²Harvard–Smithsonian Center for Astrophysics, Harvard University, Cambridge MA 02138; tdimatte@cfa.harvard.edu

³OAB Brera, Italy; belloni@merate.mi.astro.it

⁴NASA MSFC, SD-50, Huntsville, AL 35812; kouveliotou@eagles.msfc.nasa.gov

⁵*Chandra* fellow

1. Introduction

Quasars and other Active Galactic Nuclei (AGN) are generally thought to be powered by accretion onto supermassive black holes at the centers of galaxies. They are well-studied across the full astronomical bandpass, from radio to gamma-ray wavelengths. At X-ray energies, attention in recent years has focused on the broad Fe K α fluorescence line seen in many AGN of the Seyfert 1 type (for a recent review, see Fabian et al. 2000). At the high spectral resolutions first achieved with the *ASCA* satellite, the line in these sources is revealed to have a strongly asymmetric profile that is consistent with emission from the innermost radii of a relativistic accretion disk (Tanaka et al. 1995; Mushotzky et al. 1995; Nandra et al. 1997). The theory for the emission mechanism holds that the X-rays originate by inverse-Compton processes acting in a hot corona above a cold (weakly ionized) accretion disk that produces thermal emission in the optical and ultraviolet; thus the theory is bolstered by observations of a reflected continuum above \sim 10 keV that flattens the intrinsic inverse-Compton power-law.

Within our Galaxy, radio and X-ray observations over the course of the past six years have identified a population of X-ray binaries, the galactic microquasars, that are similar to AGN in a number of important respects. First, these sources exhibit relativistic radio-emitting outflows (e.g., Mirabel & Rodriguez 1994) analogous to the megaparsec-scale radio jets of AGN. Second, the sources are thought to harbor black hole primaries: they exhibit the canonical X-ray spectral states of black hole candidates (BHCs; see discussion below), and when dynamical mass estimates have been obtained they have supported this hypothesis (e.g., Orosz & Bailyn 1997). Finally, the sources exhibit strong X-ray variability on a broad range of timescales (hundreds of hertz to hundreds of days), also analogous to AGN. The name “microquasar” refers approximately to the relative mass difference between the two classes of object: the \sim 10 M_\odot masses of the microquasars, on the one hand, and the 10^7 – 10^9 M_\odot masses of AGN, on the other. This relative mass scale in turn is expected to set the relative variability timescale.

In addition to the properties mentioned above, an important common characteristic of the microquasars (without yet an analogue in AGN) are X-ray quasi-periodic oscillations (QPOs) in the 30–300 Hz frequency range. These QPOs have been identified in the sources GRS 1915+105 (Morgan, Remillard, & Greiner 1997), GRO J1655–40 (Remillard 1997), XTE J1550–564 (Remillard 1999), XTE J1748–288 (Fox & Lewin 1998; Revnivtsev, Trudolyubov, & Borozdin 1999), and 4U 1630–47 (Cui et al. 1999a). The phenomenology of these QPOs is remarkably rich and continues to challenge both the observers seeking to characterize them (e.g., Reig et al. 2000; Sobczak et al. 2000), and the theorists seeking to explain them (e.g., DiMatteo & Psaltis 1999; Lehr, Wagoner, & Wilms 2000).

Not surprisingly, the microquasars have also been found to be a rich arena in which to study accretion physics and geometry via X-ray spectral features. *Rossi X-ray Timing Explorer (RXTE)* (Bradt, Rothschild, & Swank 1993) Proportional Counter Array (PCA; Jahoda et al. 1996) observations of XTE J1550–564 are well-fit by including a Gaussian line feature at 6.5 keV with fixed width of 1.2 keV (FWHM) (Sobczak et al. 1999). Two line features, one at \sim 5.7 keV and one at \sim 7.7 keV, were observed in the 1996 outburst of 4U 1630–47 (Cui, Chen, & Zhang, 1999). The two lines are attributed to Doppler shifting of neutral Fe K α in either a Keplerian accretion disk or bipolar outflow. Church & Church (2000) report likely Fe K α emission from four spectra taken from GRO J1655–40.

XTE J1748–288 was discovered with the *RXTE* All Sky Monitor (ASM; Levine et al. 1996) on 4 June 1998 (Smith et al. 1998). Radio observations undertaken with the Very Large Array (VLA) revealed an unresolved radio source with position coincident to that of the X-ray source (R.A. $17^{\text{h}}48^{\text{m}}05^{\text{s}}.06$, Dec. $-28^{\circ}28'25''$, J2000; Hjellming et al. 1998a). Subsequent radio observations revealed an extended source, exhibiting components with proper motion of 20–40 mas day $^{-1}$ (Rupen, Hjellming, & Mioduszewski 1998). Based on a 21-cm HI absorption measurement the distance to the source was estimated to be \geq 8 kpc, implying that the intrinsic velocity of the jet components must be higher than $0.93c$ (Hjellming et al. 1999b). QPOs with centroid frequencies of \sim 0.5 Hz and \sim 32 Hz were reported in the power density spectrum (PDS) from 6 June 1998 (Fox and Lewin, 1998). The combination of relativistic radio jets and X-ray QPOs secured the identification of XTE J1748–288 as a Galactic microquasar. Multiple observations of the source were made with *RXTE* (Revnivtsev, Trudolyubov, & Borozdin 1999) and *ASCA* (Kotani et al. 2000); the source flux decayed below the ASM detection limit in September 1998.

The evolution of black hole X-ray binary (BHXB) outbursts is generally described in terms of several canonical spectral states, distinguished by the relative contribution from low energy and high energy X-rays within the 1–10 keV band. Typically, low energy X-rays (1–2 keV; the soft component) dominate the emission of a BHXB outburst near maximum, and as the outburst evolves the soft component grows weaker. Higher energy X-rays (5–10 keV; the hard component) become stronger and dominate as the overall flux decreases in the late stages of a BHXB outburst.

The canonical BHXB spectral states are the Very High State (VHS), the High or Soft State (HS), the Intermediate State (IS), the Low or Hard State (LS), and the Quiescent State (QS). In the LS, the X-ray spectrum is nearly a pure power-law, with photon index 1.5–2.5, often extending to hundreds of keV (Tanaka & Lewin 1995). In the HS, the 1–10 keV flux is an order of magnitude higher than in the LS due to the addition of a strong soft component. In the VHS the soft component is stronger still and may be accompanied

by a substantial hard component; in addition, QPOs are often observed in this state. The IS is a transitional state between the LS and the HS (Mendez & van der Klis, 1997), not observed in all sources. Finally, the QS state is typified again by a non-thermal spectrum, with a flux level several orders of magnitude below the lowest (LS) outburst flux.

Although the temporal and spectral behavior of BHXBs has been widely studied, the mechanism driving the state transitions is still unknown. The quasi-thermal radiation present in the VHS, HS, and IS is typically modeled as thermal emission from an optically-thick, geometrically-thin, multi-temperature accretion disk (Mitsuda et al. 1984). The power-law component, meanwhile, is generally attributed to inverse-Compton processing of lower-energy disk photons in an optically-thin corona above the accretion disk (Sunyaev & Titarchuk, 1980). If signs of hardening in the spectrum above ~ 10 keV are present and accompanied by a fluorescent Fe K_{α} line, then – much as in AGN – these can be interpreted as the signature of Compton reflection from the cold matter in the disk (George & Fabian 1991).

Reflection features in the LS of BHXBs, however, are generally much less prominent than in AGN (Zycki et al. 1999), so it has been argued that at least in the LS, the geometrically-thin disk does not extend inward to the innermost stable orbit, but is truncated at hundreds or thousands of Schwarzschild radii (Esin et al. 1997). In the HS, the optically thick disk is postulated to move inwards so that the majority of the dissipated energy emerges in the form of a blackbody-like spectrum. Measuring reflection spectra in BHXBs may therefore be helpful in understanding the physical properties of BHXB accretion geometries.

Previous analysis of *RXTE* observations of XTE J1748–288 revealed Fe K_{α} emission in the LS spectra of this source (Revnivtsev, Trudolyubov, & Borozdin 2000). Our fits to the same data revealed a strong LS iron feature, and in addition we found that it was possible to trace the feature backwards into the HS, and even the VHS. Here we present the results of 22 X-ray spectral observations spanning ~ 120 days of the 1998 outburst of XTE J1748–288. We investigate relativistically-skewed emission features and disk reflection in the spectra from this source.

2. Observations and Spectral Analysis

2.1. Observations

We include all of the publicly-available *RXTE* TOO data between peak bolometric luminosity and quiescence in our analysis. This embodies 22 pointed observations,

effectively sampling the different spectral states across the outburst; see Table 1 for times and ObsIDs of these observations. The standard FTOOLS v.4.2 package was used to reduce the Standard-2 PCA data from these observations. All observations were dead-time corrected, and the background was calculated using the Very Large Events (or Bright Source) option within PCABACKEST.

2.2. Gain Drift and Response Matrices

The *RXTE* PCA instrument (Jahoda et al. 1996) consists of 5 individual proportional-counter detectors, the proportional counter units (PCUs). Due to gas exchange between propane and xenon layers in the detectors, the gain of the individual PCUs drifts. PCUs 0, 1, and 4 have very similar gain drift patterns, and a better overall performance than PCUs 2 and 3 (Sobczak et al. 1999; Church & Balucinska-Church 2000). We have chosen to fit data from all layers (all propane layers and all xenon layers) of PCUs 0, 1, and 4 simultaneously.

Analysis of the data from an May 1998 observation of the Crab nebula with the response matrices calculated via the Ftool PCARMF (v3.5) shows substantial residual trends. These deviations are thought to represent defects in the response matrices themselves as the Crab is known to have a featureless power-law spectrum. We use response matrices generated by PCA calibration specialist Keith Jahoda that eliminate these residuals. They are available through the Goddard Space Flight Center ftp archive at ftp://lheaftp.gsfc.nasa.gov/pub/keith/response_matrices_v2.2.1_v80.tar. A comparison of the data/model ratio using PCARSP-generated and Jahoda-generated (hereafter “static”) response matrices, presented in Fig. 1, reveals that the static response matrices yield a much cleaner fit to the Crab data in the 3.5–10.0 keV band. For this reason, we use the static response matrices for all spectral fits.

2.3. Calibration via the Crab Nebula

We have analyzed every non-slewing observation of the Crab nebula from May to October 1998 to check for variations in the performance of the static response matrices over time.

These Crab fits were used to select an appropriate energy range for precision analysis of the data from XTE J1748–288. The bins between 2.0 and 3.5 keV varied drastically and randomly in fits to these Crab observations: the χ^2 statistic for these bins consistently fell in the range of \sim 40–100. Therefore, we set a lower energy limit of 3.5 keV for our analysis.

Above \sim 20 keV, neither type of response matrix satisfactorily fits the Crab. As this energy is high enough to constrain reflection features fit to the data, we fix 20 keV as the upper limit of our fitting range.

The addition of 1% systematic errors has become a standard practice when reducing PCA spectral data (see, e.g., Cui, Chen, & Zhang, 1999; Sobczak et al. 1999). Fits to the set of Crab observations mentioned above with this 1% systematic error produced artificially low χ^2 values. We find that a systematic error of 0.75% yields fits to the Crab observations with $0.99 < \chi^2/(dof) < 1.0$; we therefore adopt this systematic error value for our fits. This step adds validity to the measures of statistical merit based on $\Delta(\chi^2)$ that we employ in our analysis.

2.4. PCA Calibration Sources

Onboard the PCA are several pellets of radioactive Americium, ^{241}Am , that are used for in-flight calibration. Data from these sources is accumulated every 128 seconds and telemetered as part of the Standard1 data. As the line emission energies of the source are precisely known, any drift in the measured energy of the lines over the lifetime of the satellite can be directly attributed to changes in the detector response.

We collected all of the calibration source data from the first (4 June) and last (26 September) days on which XTE J1748–288 was observed; analyzing this data in channel space we find that the centroids and widths of the ^{241}Am lines agree to $<1\%$ and $<2\%$, respectively, for these two days. We therefore expect that the PCA energy scale drift is less than 1% over the time *RXTE* conducted these observations. Assuming a linear scale, this represents a systematic drift of ≤ 0.06 keV for a line feature centered at 6.0 keV.

2.5. ASCA-measured N_H

As we determined, *RXTE*’s effective sensitivity range does not extend below 3.5 keV during the time of our observations. We therefore rely on *ASCA* observations to measure the column density reliably. Kotani et al. (2000) report $N_H = 9.0 \times 10^{22} \text{ cm}^{-2}$ for a power-law index of $\alpha_{pl} = 2.9$, and N_H at $6.0 \times 10^{22} \text{ cm}^{-2}$ for $\alpha_{pl} = 2.7$, each with an error of approximately $\pm 30\%$. Both of these ASCA-measured power-law indices agree with the power-law indices we measure using *RXTE* data. We therefore fix the value of $N_H = 7.5 \times 10^{22} \text{ cm}^{-2}$ for all of our fits.

2.6. Fitting Method

Our spectral fits progressed through three increasingly complex spectral models, a process which we illustrate for two representative observations (obs. 3 and 19, from the VHS and LS, respectively) in Figure 2.

First, we fit the data with the canonical multicolor blackbody disk plus power-law model (top and second panels in Figs. 2a and 2b). The most striking feature in the data/model ratio plots for this model (second panel) is a broad excess between 4 and 7 keV for Obs. 3, and a distinct 6.7 keV line for Obs. 19. Our second model therefore adds one (Fig. 2b) or two (Fig. 2a) Gaussian components to the underlying continuum (third panel). In the case of Obs. 19 (and other LS observations), the fit is further improved by addition of a Gaussian at 8 keV (fourth panel in Fig. 2b); we discuss this feature in more detail in Sect. 3.2 below.

Two spectral features are expected to result from the reflection of hot X-rays from an accretion disk: fluorescent line emission, and a broad Compton-upscattering excess often referred to as a “reflection bump.” To be self-consistent, our final model (bottom panels in Figs. 2a and 2b) therefore consists of the multicolor blackbody disk (Diskbb) component, two Gaussians, and a Pexriv component (Magdziarz & Zdziarski 1995). Pexriv incorporates an incident power-law source of photons, and the reflection of these photons off an ionized disk. For all fits with Pexriv, we fix the power-law cutoff energy at 200 keV, and the disk inclination at 45 degrees (as we do for disk line profiles). We report measurements of the disk reflection fraction ($f = \Omega/2\pi$) and ionization ($\xi = L_x/nr^2$). Pexriv reduces to a simple power-law in the absence of reflection.

We report the results of our continuum and Gaussian-line fits in Tables 2 and 3, respectively.

Models for emission line propagation from a relativistic spacetime generally predict a double-peaked line profile (see, e.g., Dabrowski et al. 1997, Martocchia et al. 2000). Noting that the double-peaked nature of the soft emission excess in the VHS might be due to relativistic skewing, we attempted to fit these spectra with a relativistic line feature, the Laor model from XSPEC (Laor, 1991). This is a general model and may be applied to Kerr geometries but reduces to a Schwarzschild geometry in the minimal angular momentum limit. In the absence of optical or radio data to constrain the disk inclination angle, we fix this parameter at 45 degrees. In addition, the disk emissivity profile is fixed at r^{-2} , the inner emission radius of the disk to $1.235 R_g$ (as for a nearly-maximally rotating Kerr black hole), and the outer emission radius to $50.0 R_g$. The gravitational radius R_g is GMc^{-2} , where G is Newton’s gravitational constant, M is the mass of the compact object, and c is

the speed of light (R_g is half of the Schwarzschild radius). Measurements of the inner disk radius in the VHS are reported in Table 4.

In the LS, models for accretion flow around black holes (Esin et al. 1997) suggest that the inner edge of the accretion disk does not extend as far inwards as in the VHS. Measurements of the inner disk radius derived from the normalization of the multicolor blackbody disk component suggest the same phenomenology. It follows that emission from the inner disk regions in the LS would not suffer the same degree of relativistic skewing. Thus, an additional fit is made to LS spectra with a model consisting of the “Diskline” line emission model within XSPEC (Fabian et al. 1989) and Pexriv. For these fits, we fix the disk emission profile to r^{-2} and the disk inclination to 45 degrees; and the outer disk radius to $10^4 R_g$. We fit for inner disk radius, line centroid energy, and the component normalization. The results of fits using this model are reported in Table 5.

3. Results

3.1. Continuum Components

The total 3.5–20.0 keV flux measured using our models peaks at 11.4×10^{-9} ergs cm^{-2} s^{-1} between outburst days 2 and 8, and is dominated by the hard power-law component. The soft multicolor disk blackbody flux is slightly less than half of the hard power-law flux in observations 3 and 4, but a smaller fraction in observations 5–8 (see Table 2). The normalization of the blackbody disk component is tightly constrained in this state, and is relatively constant. These relative flux measurements and very high overall flux level signify that XTE J1748–288 is in the VHS during observations 3–8. The disk blackbody temperature is well-measured, and decreases very slightly through this state, from 1.57 to 1.26 keV. The normalization of the hard power-law component is well-constrained; the spectral index hardens through the VHS (see Table 2, Figure 4a).

Between observations 8 and 9, the hard power-law flux falls and the 3.5–20.0 keV spectrum becomes dominated by the soft component. The multicolor blackbody disk flux increases by a factor of ~ 4 between these observations. We interpret this change in continuum component flux as the VHS to HS transition. The blackbody disk temperature decreases from 1.29 to 0.91 keV through this state (see Table 2). The normalization of the soft component peaks mid-way through the HS, dipping most dramatically in observation 15, just prior to the HS–LS transition. The power-law spectral index is softer than in the VHS at the beginning of the HS, but the index steadily hardens through the HS. Whereas the soft blackbody disk normalization peaks mid-way through this state, the hard power-law

component normalization falls steadily throughout (see Table 2).

The multicolor blackbody disk temperature falls by half between observations 15 and 16, and the soft flux is nearly extinguished. This marks the HS to LS transition. Ginga observations of GS 1124–68 (Ebisawa et al. 1994) and GS 2023+338 (Zycki et al. 1999) yield LS disk temperatures of ~ 0.3 keV. We measure a disk component with similarly low temperature in observations 16, 17, and 18, but find no evidence of a disk flux in subsequent observations. It is therefore possible that the disk cools to a temperature well below the range of sensitivity of the PCA. The power-law spectral index is uniformly harder ($1.86 \leq \alpha_{pl,LS} \leq 2.08$) in the LS than in any observation in the VHS or HS. The normalization of the power-law component decreases throughout the LS, as does the overall flux. The power-law index measured with Pexriv hardens steadily, slightly increasing in the last two observations (see Table 2, Figure 4b).

The multicolor blackbody disk model yields an inner accretion disk radius, with component normalization, source distance, and disk inclination as parameters. Fits with this model indicate that the inner disk radius is relatively constant at ~ 10 km in the VHS, and ~ 19 km for every observation made in the HS (see Table 4).

3.2. Line Components

Figures 3a and 3b show data/model ratios for the VHS and HS, and LS, respectively. The ratios are off-set from each other, but on the same relative scale. The models used here are the multicolor blackbody disk plus Pexriv for the VHS and HS, and Pexriv only for the LS. These figures serve to illustrate how the equivalent width, width, and centroid energy of the line features detailed in Table 3 vary across the outburst.

The bottom data/model ratio plot in Figure 3b corresponds to observation 23, just before the source slipped beneath RXTE detection limits. The line feature is very strong, broadened, and single-peaked. Tracing backwards to the beginning of the LS (top of Figure 3b), it is readily apparent that the line centroid energy is approximately constant, and the equivalent width is diminished in earlier observations. The width of the line feature is measured to be ~ 0.30 keV throughout, indicating that the line is resolved by the PCA in the LS (see Table 3).

The resolved line in the LS allows for tightly-constrained measurements via fits with the Diskline model. Centroid energy values fall within ± 0.1 keV of 6.7 keV, and the line equivalent width increases steadily from $\sim 200 \pm 20$ eV to $\sim 916 \pm 33$ eV. These measurements are in good agreement with the values obtained by fitting the line with a

Gaussian profile. Most notably, the Diskline model measures the inner edge of the accretion disk, which remains relatively close to the innermost radius in the LS. Our fits indicate the inner edge of the disk is moving closer to the BH in observations 16, 17, and 18, from $63^{+933}_{-31} R_g$ to $\sim 60^{+15} R_g$. The inner edge then recedes back to $102^{+140}_{-63} R_g$ in observation 19. Following this sharp recession, we measure the inner disk radius to move steadily inward in subsequent observations, to $\sim 35^{+34}_{-15} R_g$ in observation 23.

Fits to the LS are improved by adding a higher-energy Gaussian line component to the spectral model at ~ 8.3 keV. This unresolved line feature is suggested at $>68\%$ confidence throughout the LS, and is consistent with fluorescent Ni $K\alpha$ emission from a highly-ionized species. The equivalent width of this line varies between 10–260 eV from observation 16 to observation 23. The presence of this line feature is visible in Figure 2b once the more intense line at ~ 6.7 keV has been fit, but is not visible in the plots in Figure 3b as it is far less intense than the lower energy line.

Following the data/model ratio from the beginning of the LS (top of Figure 3b) to the end of the HS (bottom of Figure 3a), the ~ 6.7 keV line feature is still very prominent, and can in fact be traced all the way back to the VHS (top of Figure 3a). Although the line feature is much weaker in the VHS than in the HS or LS, the constancy of the centroid energy and smooth evolution of the equivalent width clearly tie the line emission feature near ~ 6.7 keV in the HS and VHS to that in the LS.

A lower-energy line feature is present in the HS that is not seen in the LS. We distinguish these HS and VHS features as the “red” and “blue” lines. Fitting a model including two Gaussian lines to the HS, we find that the blue line feature is significant at greater than 90% confidence in all but one observation in the HS (obs. 10). The centroid energy of the blue line slowly increases from 6.4 to 6.7 keV from the beginning to the end of the HS. The equivalent width also increases steadily, from 39 to 347 eV (see Table 2, Fig. 4a). The red line is not significant at 90% confidence in obs. 10, but is measured in the three observations at the beginning of the HS.

Again tracing backwards in time (bottom to top) in Figure 3a, the rising equivalent width of the red component and the smeared profiles of both red and blue line features is clearly seen. In the VHS the line emission feature may be characterized as smeared and possibly double-peaked. Fits to the VHS spectra with a model including two Gaussian line emission features find the red line is significant at $>99.9\%$ confidence for every observation. The blue line is significant at $>99.9\%$ in all but obs. 6. Generally, the equivalent width and flux of the red line are greater than that of the blue line in the VHS.

The red line centroid energy decreases slightly through the VHS, but is consistent with

4.6 keV (see Fig. 4a). The centroid energy of the blue line varies in the VHS, steadily increasing from 5.8 to 6.6 keV (see Table 3). The red line width is inconsistent with zero in the VHS except in observations 3 and 6; the blue line except in observation 7. The red line is likely at the limit of the PCA resolution in the VHS; it is unresolved in the HS. The blue line is especially broad (0.8 keV) at the beginning of the VHS, becoming narrower throughout (to 0.4 keV in obs. 8).

Fits with the Laor relativistically-skewed line emission model show that the addition of a line feature emitted from a region between $1.2 R_g$ and $30.0 R_g$, with centroid energy of 5.7 keV, is significant at 90% confidence in observations 3, 4, and 8. Later observations cannot be fit as well with the Laor model. Indeed, we do not expect that the resolution of the PCA is sufficient to constrain Laor model parameters; fits with this model serve primarily as a consistency check.

The continuity of the changes in line parameters and profiles as we search backwards from the LS to the VHS indicates that the line-like excesses seen in Figures 3a and 3b are very likely manifestations of the same line emission feature.

Tracing the line feature(s) backwards in time from the LS, the equivalent width is observed to steadily decrease. It is important to note that the flux in the red line feature in the VHS is greater than the flux in the single-peaked/blue line feature in the LS (see Table 3). Considering the states separately, the flux of the lines is highest at the beginning of each spectral state, and gradually decreases throughout (see Table 3, Fig. 4). More generally, the lines have the highest flux in the VHS at the beginning of the outburst. The line profile is possibly double-peaked in the VHS. As the outburst moves into the HS, the line profile becomes single-peaked and increases in equivalent width, though the line flux decreases steadily. Finally, as the outburst moves into the LS, the line equivalent width becomes very large (the soft blackbody disk continuum component disappears) and the line flux continues to decrease steadily.

Revnivtsev, Trudolyubov, & Borozdin (1999) only find evidence for a line component in the LS spectrum of XTE J1748–288, and suggest that the line is from diffuse galactic emission as the line flux is stable relative to the decline in the power-law flux. We disagree with this interpretation. Our finding that the line flux is highest at the beginning of each spectral state and decays until the end of the state demands that the spectral lines are produced by XTE J1748–288.

3.3. Reflection

The power-law continuum component Pexriv models the reflection of hot X-rays impinging on an ionized, optically-thick gas, often assumed to be an accretion disk. In the VHS, the reflection fraction f is small but non-zero at $>90\%$ confidence (except obs. 6; see Table 2, Fig. 4a). Measurements indicate that the disk is very ionized at the beginning of the VHS ($\xi \sim 7000$ in obs. 3). The ionization is constrained only in observations 3, 4, and 5. Thereafter in the VHS, and throughout the LS, the ionization is not tightly constrained but a highly-ionized disk is preferred at 90% confidence. We therefore fixed the ionization ($\xi = 2000$) in fitting observations 6–15.

Across the VHS–HS transition, f varies discontinuously from ~ 0.04 in observation 8 to ~ 0.01 in observation 9. Throughout the HS, f increases to a value of ~ 0.11 in obs. 15. Perhaps due to the dominance of the soft component in the HS, f is consistent with no reflection throughout.

The reflection fraction f again varies sharply across the HS–LS transition, from ~ 0.11 in observation 15 to 0.45 ± 0.02 in observation 17. The value of f falls sharply in subsequent observations, to ~ 0.04 in observation 21, and becomes consistent with zero in obs. 23 (see Table 2, Fig. 4b). Measurements of ξ in the LS are consistent with a neutral disk, marking a sharp contrast to the highly-ionized disk required in the VHS and HS.

4. Discussion

4.1. The Fe K α Fluorescent Line

Based on the broadened, redshifted line emission profile observed by Iwasawa et al. in MCG–6–30–15 (1997), and on the profiles and equivalent widths calculated by many researchers (e.g. Magdziarz & Zdziarski 1995, Fabian et al. 1989, George & Fabian 1991, Dabrowski et al. 1997, Martocchia et al. 2000), we interpret the red and blue line features in the VHS of XTE J1748–288 as wings of a Doppler- and gravitationally-shifted Fe K α line emission profile. The line profiles (Figs. 2a and 3a; Table 3) are consistent with those calculated by Martocchia et al. (2000) for emission from the innermost region of an accretion disk orbiting a BH of high angular momentum, viewed at a modest inclination angle, with a source of hot X-rays located $\leq 10 R_g$ above the BH. The equivalent widths measured in the VHS are broadly consistent with those predicted by the model for a disk with outer emission radius near $100 R_g$, and viewed at an angle slightly below the 45 degree inclination we assumed.

Our fits to the VHS using the Laor model indicate that in this spectral state the relativistically-skewed line is consistent with emission from an inner radius extending down to the marginally stable orbit for a maximally rotating Kerr black hole, $1.2 R_g$ (see Table 4), in obs. 3 and obs. 4. Measurements of the inner disk radius via the multicolor blackbody disk model in the VHS confirm that the disk may extend to the innermost stable orbit in a Kerr geometry (see Table 4).

Throughout the HS, the red wing of the profile becomes less prominent, and the blue wing strengthens. In particular, the centroid energy of the blue line shifts from 5.8 keV (beginning of the VHS) to 6.7 keV (end of the HS). Throughout the LS, the line profile is single-peaked, and measured at 6.70 ± 0.10 keV. This value is consistent with highly ionized species of iron. We suggest that this line is likely a complex of lithium-like, helium-like, and hydrogenic iron species (Fe XXIV-XXVI). The shift of line profile to higher centroid energies may be produced in two ways, either by an evolving ratio of iron ionizations contributing to the line profile, or by the disk mildly recessing from the BH. Given the inner disk radii we measure (see Table 2) across the outburst and the high ionization preferred in the VHS and HS, it is likely that the latter process dominates, but both may contribute.

Although unlikely given the relatively continuous evolution of the line profile (in contrast to the discontinuous nature of the jet, which is only reported in the VHS), it is nevertheless possible that the lines originate within the jet itself. It is also possible that the lines are produced within a hot coronal region, and the measured reflection is from a cold geometry apart from the disk.

4.2. Disk Reflection and Ionization

The reflection fractions we measure in the VHS and HS are smaller than the same parameter measured in observations of other BHXBs and AGN. Done, Madejski, & Zycki (2000) measure f between 0.55 – 1.25 in Seyfert 1 galaxy IC4329a. Zycki, Done, & Smith (1998) measure $f \sim 0.30$ in the VHS, and $f \sim 0.64$ in the HS of the 1991 outburst of GS 1124–68. Zycki et al. (1999) measure $f \sim 0.4 – 0.9$ during the decline of GS 2023+338 (this source was dominated by the hard power-law component through its decline, unlike XTE J1748–288 and GS 1124–68). The reflection fraction measured in the early LS observations of XTE J1748–288 is comparable to that measured in the LS of Cygnus X-1 by Gierlinski et al. (1999) $f_{cyg,LS} \sim 0.5 – 0.7$.

The low reflection fractions we measure are likely due to the high disk ionizations strongly preferred in the VHS and HS. The contrasting high reflection and negligible

ionization at the beginning of the LS is not surprising; a similar phenomenology is noted by Zycki, Done, & Smith (1998) for the HS-LS transition in GS 1124–68. In a geometry where the disk is illuminated by a central source of hot X-rays, the disk should be most ionized when the hard X-ray flux is highest and when the disk is closest to the central source. The hard X-ray fluxes and inner disk radii measured in XTE J1748–288 support this picture. Moreover, the lines that we measure in the VHS and HS, though often significant at 99.9% confidence, are still weaker than those seen in AGN spectra. Therefore, the strength of the two components predicted for reflection spectra – fluorescent line production and disk reflection, are at least qualitatively consistent.

Ross, Fabian, and Young (1999) note that even the small departures from uniformity that may occur in a highly ionized disk can account for the small reflection fraction often observed in such scenarios, without invoking reflection from the outer disk. This research, and that of Nayakshin, Kazanas, & Kallman (1999) finds that the hottest outer layers of the accretion disk are important in accurately determining disk reflection fractions. These studies find that Pexriv may be too basic in its treatment of Compton processes in these hot outer layers. At present, Pexriv is the best code publicly available. We look forward to the release of more sophisticated codes and to high resolution data from Chandra and XMM-Newton to constrain new models.

We also note that we are only able to obtain measurements for the reflection fraction inconsistent with zero when the hard flux dominates the 3.5–20.0 keV bandpass we fit. This condition is met throughout the VHS, in obs. 15 in the HS, and throughout the LS. With the exception of obs. 15, we are not able to place tight constraints on reflection in the HS. Many models for disk reflection are based upon AGN spectra (the codes we mention above are notable exceptions), which generally do not contain a soft component in the X-ray band. The extent to which the physical process of soft X-ray emission from the disk is responsible for confusing disk reflection measurements, relative to merely poor mathematical modeling, is unknown.

4.3. Implications for Geometry and Accretion Flow

DiMatteo & Psaltis (1999) establish a possible connection between QPO frequency and inner disk radius in BHXBs based on similar work on neutron star (NS) systems:

$$\left(\frac{R_{\text{in}}}{R_g}\right) \leq 27 \nu_1^{-0.35} \left(\frac{M}{2M_\odot}\right)^{-2/3}, \quad (1)$$

where ν_1 is the QPO frequency, R_{in} is the inner disk radius, R_g the gravitational radius, M the mass of the black hole, and M_\odot a solar mass. For a measured QPO frequency, and a measured or assumed black hole mass, the inner radius can be determined via this equation. Inserting the 32 Hz QPO (Fox & Lewin, 1998) measured in the VHS of XTE J1748–288, and assuming a black hole mass of $10M_\odot$, this equation predicts an upper limit for the accretion disk inner radius of $\sim 2.75 R_g$. This value supports the measurements we obtain via the Laor line model, and our comparison to the models of Martocchia et al. (2000).

The multicolor blackbody disk continuum model also provides a measure of the inner disk radius. A central black hole with a mass of $10M_\odot$ has a gravitational radius of ~ 15 km; a central black hole with mass $5M_\odot$ a gravitational radius of ~ 7.5 km. Fits using the multicolor blackbody disk model measure the inner disk radius in the VHS to be ~ 10 km. Fits with the Laor disk line emission model in the VHS are consistent with an inner disk radius extending down to $1.2R_g$; this corresponds to ~ 18 km for $M_{BH} = 10M_\odot$, and ~ 9 km for $M_{BH} = 5M_\odot$. Finally, the connection noted by DiMatteo & Psaltis (1999) suggests an inner disk radius of $\sim 2.75R_g$, or 41.3 km and 20.6 km for $10M_\odot$ and $5M_\odot$ black holes, respectively. Although these methods do not yield exactly the same inner disk radii, they all indicate that the inner edge of the accretion disk extends below the marginally stable orbit for a non-rotating Schwarzschild black hole ($R_{\text{ms,Sch}} = 6R_g = 90$ km; for $M_{BH} = 10M_\odot$, $R_{\text{ms,Sch}} = 6R_g = 45$ km, for $M_{BH} = 5M_\odot$; see Table 4 for R_{in} results).

Narayan and Yi (1994) describe a solution for BH accretion geometry wherein a hot, optically thin, inefficiently-cooled plasma advects energy directly onto the BH. Originally developed to describe the presence of hard emission within the spectra of AGN, these Advection-Dominated Accretion Flow (ADAF) models successfully describe a number of AGN (see Narayan 1997 for a review). A natural application of this model is soft X-ray transients in quiescence, where \dot{m} is sufficiently small. BHXBs V404 Cygnus and A0620-00 are well fit by ADAF models in quiescence (Narayan, McClintock, & Yi 1996; Narayan, Barret, & McClintock 1997a).

Esin, McClintock, and Narayan (1997) describe an ADAF/thin-disk composite model tuned to explain the full spectral state evolution of BHXBs over a range of luminosities and \dot{m} . The parameter which drives the spectral transitions is the location of the ADAF/disk transition radius, R_{tr} . When R_{tr} is close to the BH, the emission is dominated by the disk. As the outburst evolves, cooling becomes less efficient, \dot{m} falls, the inner region becomes an ADAF, and R_{tr} increases. Esin et al. predict that in the VHS and HS, the disk may extend to the innermost stable orbit, but in the LS and QS R_{tr} is likely to be near $\sim 10^4 R_g$. This model is applied to the 1991 outburst of GS 1124–68, and describes all but the VHS. Subsequent application of the model to Cygnus X-1 in its LS indicates $R_{tr} \sim 100 R_g$ (Esin

et al. 1998).

Zycki, Done, & Smith (1998) constrain the hot advection zone to lie within $\sim 20-100 R_g$ in the LS of GS 1124–68, based on smearing of the Compton upscattering excess observed above ~ 10 keV. The inner radii we measure in the LS of XTE J1748–288 via the multicolor blackbody disk model and the Diskline relativistic line model also constrain the inner disk edge to lie in this range. We therefore conclude that a large ($10^4 R_g$) inner advection region of the kind predicted by Esin, McClintock, and Narayan is not consistent with the LS of XTE J1748–288 but must be within $100 R_g$ (similar to Cygnus X-1) if such a geometry exists.

We make note of work by Merloni, Fabian, & Ross (2000), which finds that the multicolor blackbody disk model systematically underestimates the real inner disk radius, and can suggest inner disk motion at high accretion rates when in fact the disk is stable at the marginally stable orbit. In the VHS, we find that the multicolor blackbody disk radius is stable and corresponds to the marginally stable orbit for a Kerr black hole (see Table 4). The radii we measure via this model in the VHS are supported by radii derived via DiMatteo & Psaltis (1999), but may be an important caveat for HS measurements.

4.4. Constraints on the BH Mass

Combining the relation discussed by DiMatteo & Psaltis with the multicolor blackbody disk normalization in the VHS and the radio-band distance estimate, we obtain the following constraint for the mass of the central object in XTE J1748–288:

$$M \geq 7.9 M_\odot \left(\frac{D}{8 \text{ kpc}} \right)^3 \left(\frac{\cos \theta}{\cos 45^\circ} \right)^{-3/2} \left(\frac{N}{100} \right)^{3/2} \left(\frac{\nu}{32 \text{ Hz}} \right)^{1.05}, \quad (2)$$

where M is the mass of the compact object, M_\odot the solar mass, D the distance in kiloparsecs, N is the normalization of the Diskbb component (see Table 2), θ the disk inclination angle, and ν the QPO frequency. Although this calculation is subject to numerous uncertainties, including the uncertain color correction (Ebisawa et al. 1994), taken at face value it implies a black hole primary ($M > 4.5 M_\odot$) in XTE J1748–288 for a large parameter space including all likely values of D (> 8 kpc from radio measurements) and $\cos \theta$ (< 1).

4.5. Comparison to Recent Evidence of Lines in BHXBs

Cui, Chen, & Zhang (1999) find two co-moving line features placed quasi-symmetrically about 6.5 keV in the 1996 outburst of 4U 1630-47. It is suggested that each may be due to Doppler-shifted Fe K_{α} emission (not principally gravitational redshifting, in the case of the reddened line).

Church et al. (2000) report on four spectra from GRO J1655–40, and find evidence for gravitationally redshifted and Doppler-broadened emission. Our finding that the red emission wing is more prominent than the blue emission wing early in the VHS of XTE J1748–288 is qualitatively similar to these results.

Unfortunately, 4U 1630–47 and GRO J1655–40 are both known to be “dipping” sources (Kuulkers et al. 1988) – to experience periods of markedly different absorption during outburst – and this complicates efforts to trace spectral lines across a full outburst and thereby constrain accretion flow geometries. The Compton upscattering excess in XTE J1748–288 that we model with Pexriv is not discussed by these authors.

5. Conclusions

We have analyzed the 22 publicly-available observations between maximum X-ray luminosity and quiescence from the outburst of galactic microquasar BHXB XTE J1748–288. The spectra can be categorized into Very High, High, and Low States based on the relative flux contributions from hard and soft continuum components. We trace emission lines through these spectral states, and find evidence for an Fe K_{α} line that is gravitationally redshifted and Doppler shifted in the VHS, with a profile that is consistent with emission from the innermost stable orbit for a maximally rotating Kerr black hole. The line is less redshifted but increasingly prominent in the HS. Finally, in the LS, the line is centered at 6.7 ± 0.10 keV, and we measure a profile that is consistent with emission from a disk with inner radius between $R \sim 20$ and $R \sim 100 R_g$.

We fit each observation with a power-law continuum model (Pexriv) that includes Compton reflection of hot incident X-rays from an ionized disk component, manifested spectrally as a broad excess above ~ 10 keV. This work represents the first trace of the disk reflection fraction across the full outburst of a BHXB. The fractions we measure in the VHS and HS are much smaller than those often measured in AGN, but well-constrained. We note that the Pexriv model may be too basic for accurate reflection measurements, and urge the public release of new codes.

The Fe K_{α} line serves as a direct diagnostic of the accretion geometry. We consider our findings in the context of the ADAF model developed by Esin, McClintock, & Narayan (1997) to describe the spectral states of BHXBs. As the disk in XTE J1748–288 is measured to be a few tens of R_g from the BH in the LS, rather than 10^3 - $10^4 R_g$, we find that the predictions of this ADAF model are inconsistent with the accretion geometry of XTE J1748–288.

We look forward to data from Chandra and XMM to obtain higher-resolution spectra of a BHXB in outburst.

6. Acknowledgments

Special thanks is due Taro Kotani for his communication of ASCA N_{H} measurements in advance of publication.

We thank Michael Muno, Dimitrios Psaltis, Rob Fender, Keith Jahoda, Andrzej Zdziarski, and Wei Cui for numerous insights . We are especially indebted to Ron Remillard for his many helpful discussions.

WHGL gratefully acknowledges support from NASA. TDM and RW were supported by NASA through Chandra Fellowship grant numbers PF9-10005 and PF-9-10010, respectively, which are operated by the Smithsonian Astrophysical Observatory for NASA under contract NAS8-39073. This research has made use of data and resources obtained through the HEASARC Online Service, provided by the NASA-GSFC.

REFERENCES

Baluchinska-Church, M., and Church, M. J., 2000, MNRAS, subm (astro-ph/9912389)
Blandford, R. D., & Begelman, M. C., 1999 MNRAS 303L, 1B
Bradt, H. V., Rothschild, R. E., & Swank, J. H. 1993, A&AS, 97, 355
Cui, W., Zhang, S. N., and Chen, W., 1998, ApJ, 492, L53
Cui, W., Zhang, S. N., Chen, W., and Morgan, E. H., 1999a, ApJ. 512, L43
Cui, W., Chen, W., and Zhang, S. N., 1999, ApJ 529, 952
Dabrowski, Y., Fabian, A. C., Iwasawa, K., Lasenby, A. M., and Reynolds, C. S., 1997, MNRAS, 288, L11
DiMatteo, T, & Psaltis, D., 1999, ApJ 526L, 101D

Done, C., Madejski, G. M., and Zycki, P.T., 2000, astro-ph/0002023

Ebisawa, K., et al., 1994, PASJ, 46, 375

Esin, A. A., McClintock, J. E., and Narayan, R., 1997, ApJ 489, 865

Esin, A. A., Narayan, R., Cui, W., Grove, E. J., & Zhang, S. N., 1998, ApJ 505, 854

Fabian, A. C., Rees, M. J., Stella, L., and White, N. E., 1989, MNRAS, 238, 729

Fabian, A. C., Iwasawa, K., Reynolds, C. S., & Young, A. J., 2000, PASP, in press (astro-ph/0004366)

Fender, R., et al., 1999, ApJ 519, L165

Fender, R., 2000, astro-ph/9911176

Fox, D. W., & Lewin, W. H. G. 1998, IAUC 6992

George, I. M., & Fabian, A. C., 1991, MNRAS, 249, 352

Gierlinski, M., et al., 1997, MNRAS, 288, 958

Gierlinski, M., Zdziarski, A. A., Poutanen, J., Coppi, P. S., Ebisawa, K., and Johnson, W. N., 1999, MNRAS, 309, 496-512

Hjellming, R. M., et al., 1998a, IAUC 6937

Hjellming, R. M., et al., 1998b, American Astron. Soc. Meeting # 193, 103.08

Iwasawa, K., Fabian, A. C., Young, A. J., H. Inoue, & Matsumoto, C., 1999, MNRAS 306L, 19

Kuulkers, E., Wijnands, R., Belloni, T., Mendez, M., van der Klis, M., van Paradijs, J., 1998, ApJ 494 753

Jahoda, K., Swank, J. H., Giles, A. B., Stark, M. J., Strohmayer, T., Zhang, W., & Morgan, E. H., 1996, SPIE, 2808, 59

Kotani, T., et al., 1999, in X-ray Astronomy 2000, a special issue of Astrophysical Letters and Communications, in press

Laor, A., 1991, ApJ 376, 90

Levine, A. M., Bradt, H., Cui, W., Jernigan, J. G., Morgan, E. H., Remillard, R., Shirey, R. E., & Smith, D. A., 1996, ApJ, 469, L33

Magdziarz, P., & Zdziarski, A., 1995, MNRAS 273, 837

Martocchia, A., et al., 2000, MNRAS 312, 817

Mendez, M., and van der Klis, M., 1997, *ApJ*, 479, 926

Merloni, A., Fabian, A. C., & Ross, R. R., 2000, *MNRAS* 313, 193

Mirabel, I. F., & Rodriguez, L. F., 1994, *Nature*, 371, 46

Mitsuda, K., et al., 1984, *PASJ*, 36, 741

Morgan, E., Remillard, R., & Greiner, J., 1997, *ApJ*, 482, 993

Mushotzky, R. F., Fabian, A. C., Iwasawa, K., Kunieda, H., Matsuoka, M., Nandra, K., and Tanaka, Y., 1995, *MNRAS*, 272, L9

Nandra, K., George, I. M., Mushotzky, R. F., Turner, T. J., and Yaqoob, T., 1997, *MNRAS*, 476, 602

Narayan, R., McClintock, J. E., and Yi, I., 1996, *ApJ*, 457, 821

Narayan, R., Barret, D., and McClintock, J. E., 1997a, *ApJ*, 482, 448

Narayan, R., & Yi, I., 1994, *ApJ*, 428, L13

Narayan, R., 1997, in *IAU Colloq. 163, Accretion Phenomena and Related Outflows*, ed. D. T. Wickramasinghe et al., (Dordrecht: Kluwer), 75

Nayakshin, S., Kazanas, D., & Kallman, T., 2000, *ApJ* 537, 833

Orosz, J., & Bailyn, C., 1997, *ApJ*, 477, 876

Reig, P., Belloni, T., van der Klis, M., Mendez, M., Kylafis, N., & Ford, E., 2000, *ApJ*, submitted (astro-ph/0001134)

Remillard, R. A., Morgan, E. H., Greiner, J., 1997, *ApJ* 482, 993

Remillard, R. A., 1999, *ApJ*, 517, L127

Revnivtsev, M. G., Trudolyubov, S. P., and Borozdin, K. N., 2000, *MNRAS* 312 151

Ross, R. R., Fabian, A. C., & Young, A. J., 1999, *MNRAS* 306, 461

Rupen, M. P., Hjellming, R. M., and Mioduszewski, A. J., 1998, *IAUC* 8938

Smith, D., Levine, A., and Wood, A., 1998, *IAUC* 6932

Sobczak, G., McClintock, J. E., Remillard, R. A., Levine, A., Morgan, E. H., Bailyn, C. D., and Orosz, J. A., 1999, *ApJ*, L121-L125

Sobczak, G. J., Remillard, R. A., Munoz, M. P., McClintock, J. E., 2000, *ApJ*, submitted (astro-ph/0004215)

Sunyaev, R. A., & Titarchuk, L. G., 1980, *A & A* 86, 121

Tanaka, Y., et al., 1995, *Nat*, 375, 659

Takaka, Y., and Lewin, W. H. G., in “X-ray Binaries”, eds. W. H. G. Lewin, J. van Paradijs, & E. P. J. van den Heuvel (Cambridge U. Press, Cambridge)

Zhang, S. N., Cui, W., and Chen, W., 1997, ApJ, 482, L155

Zhang, S. N., et al., 2000, Science, in publication

Zycki, P. T., Done, C., and Smith, D. A., 1998, ApJ 496, L25-L28

Zycki, P. T., Done, C., and Smith, D. A., 1999, MNRAS 305, 231

Table 1: RXTE PCA Observation Log

No.	Obs.ID	Date, UT	Start Time	PCA Exp. (s)
1	30188-05-01-00	04/06/98	20:05:04	1760
2	30188-05-02-00	05/06/98	03:03:44	768
3	30171-02-01-00	06/06/98	09:41:20	2655
4	30185-01-01-00	07/06/98	07:56:32	2944
5	...-02-00	08/06/98	06:23:28	3027
6	...-03-00	09/06/98	12:48:00	3729
7	...-04-00	10/06/98	03:38:24	7721
8	...-05-00	11/06/98	12:52:16	3439
9	...-06-00	13/06/98	12:51:28	3114
10	...-07-00	15/06/98	04:53:36	1795
11	...-08-00	18/06/98	20:55:12	2327
12	...-09-00	22/06/98	22:30:08	3210
13	...-10-00	27/06/98	11:39:28	1647
13.1	...-10-01	02/07/98	18:18:24	1280
14	...-11-00	08/07/98	16:21:52	1295
15	...-12-00	13/07/98	06:44:00	2056
16	...-13-00	18/07/98	04:00:32	10585
17	...-14-00	30/07/98	09:44:48	6841
18	...-15-00	05/08/98	18:25:20	4333
19	...-16-00	13/08/98	10:17:36	1565
20	...-17-00	20/08/98	16:41:20	1704
21	...-18-00	25/08/98	03:32:00	1785
22	...-19-00	14/09/98	08:17:36	886
23	...-20-00	26/09/98	03:29:04	10287

Note. — Observations 1 and 2 are during the rise of the outburst. The remaining observations were made during the declining portion of the outburst, and are public data.

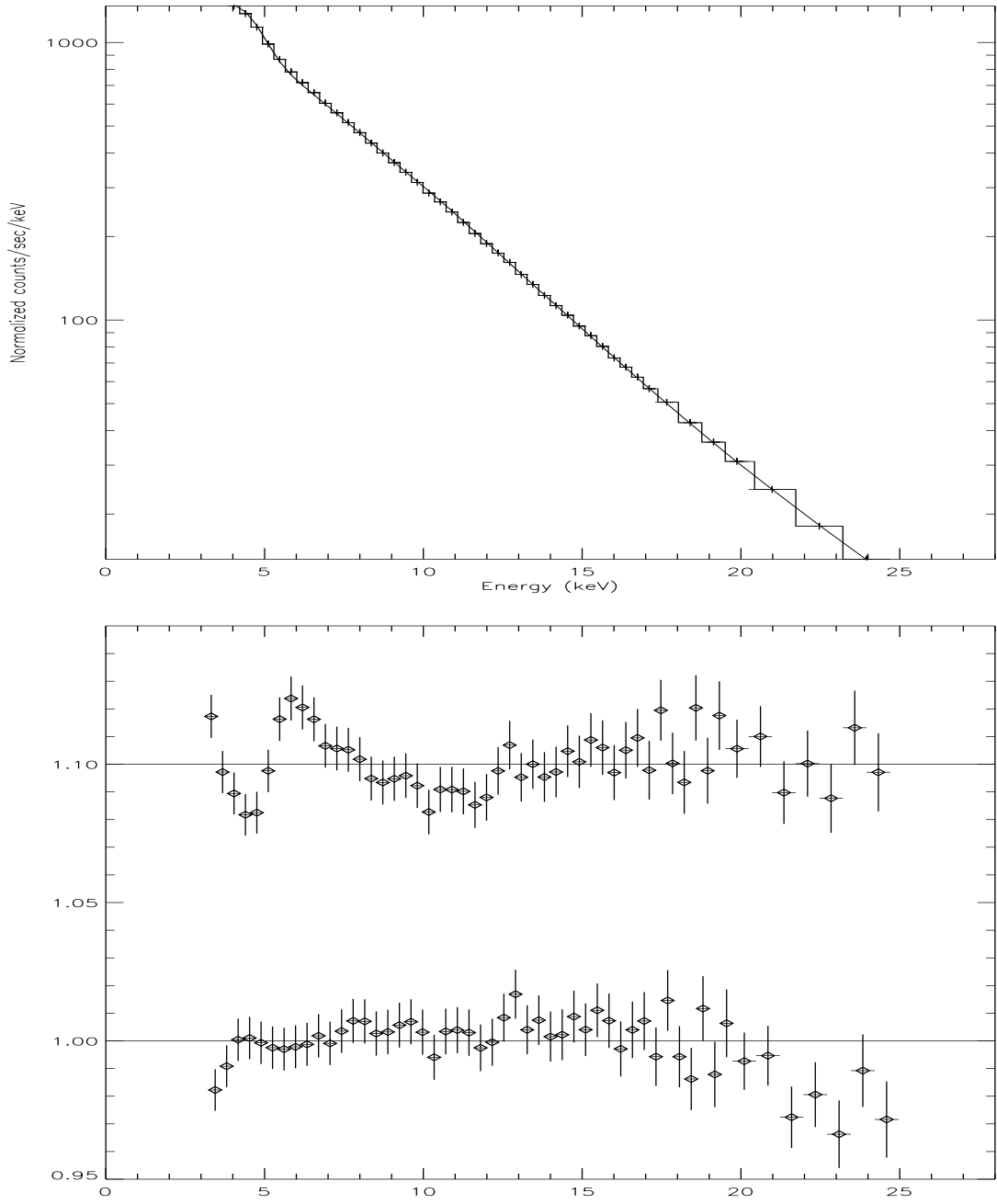


Fig. 1.— Above: May 1998 Crab Nebula spectrum, fit with power-law and low-energy absorption model. Below: May 1998 Crab data/model ratios, pcarsp (top) and static (bottom) rsp files.

Table 2: Spectral Component Parameters of XTE J1748–288

Obs.	T_{DBB} (keV)	Norm.	R_{DBB} (km)	Flux _{DBB} 10^{-9} cgs	α_{pl}	f 10^{-2}	F-stat.	ξ 10^3	Norm.	Flux _{pl} 10^{-9} cgs	Flux _{tot} 10^{-9} cgs	χ^2/dof
— Very High State —												
3	1.57(1)	90(3)	9.0(1)	3.6(1)	2.728(1)	2.1(6)	0.079	7^{+17}_{-6}	15.59(5)	7.82(2)	11.4(1)	1.02
4	1.53(1)	104(4)	9.7(1)	3.7(1)	2.736(1)	2.2(7)	0.036	3^{+8}_{-2}	15.48(5)	7.63(2)	11.3(1)	0.64
5	1.29(2)	108(9)	9.9(3)	1.5(1)	2.631(1)	2.2(6)	0.001	3^{+4}_{-2}	13.80(3)	8.43(2)	9.9(1)	0.49
6	1.19(2)	125(13)	10.6(5)	1.1(1)	2.515(1)	0.5(4)	0.403	2^\dagger	10.57(3)	8.15(2)	9.3(1)	0.45
7	1.22(2)	116(11)	10.2(4)	1.1(1)	2.571(1)	6.6(6)	<0.001	2^\dagger	11.07(2)	7.68(2)	8.8(1)	0.34
8	1.26(2)	88(6)	8.9(2)	1.0(1)	2.466(1)	3.6(9)	<0.001	2^\dagger	5.43(2)	4.64(2)	5.6(1)	0.51
— High State —												
9	1.29(1)	388(6)	18.7(2)	5.3(1)	2.73(2)	2^{+5}_{-2}	1.0	2^\dagger	3.62(2)	1.81(1)	7.1(1)	0.42
10	1.31(1)	370(6)	18.3(2)	5.5(1)	2.94(3)	2^{+12}_{-2}	1.0	2^\dagger	3.5(2)	1.15(8)	6.7(1)	0.69
11	1.26(1)	403(6)	19.1(1)	5.9(1)	2.90(6)	2^{+4}_{-2}	1.0	2^\dagger	2.1(3)	0.72(8)	6.6(1)	0.55
12	1.20(1)	436(8)	19.9(1)	3.8(1)	2.69(7)	1^{+21}_{-1}	1.0	2^\dagger	1.0(1)	0.53(1)	4.3(1)	0.70
13	1.15(1)	440(8)	20.0(1)	3.3(1)	2.58(1)	3^{+4}_{-3}	1.0	2^\dagger	0.87(8)	0.57(7)	3.9(1)	0.69
13.1	1.03(1)	450(10)	20.2(3)	1.6(1)	2.47(5)	7^{+22}_{-7}	1.0	2^\dagger	0.89(2)	0.68(1)	2.3(1)	0.45
14	0.98(1)	440(10)	20.0(3)	1.1(1)	2.41(7)	3^{+26}_{-3}	1.0	2^\dagger	0.63(7)	0.6(1)	1.7(1)	1.13
15	0.91(1)	390(10)	18.8(3)	0.56(5)	2.44(5)	11.1(1)	< 0.001	2^\dagger	0.97(1)	0.87(2)	1.4(1)	0.94
— Low State —												
16	0.42(3)	7800 ₃₇₀₀ ⁷⁵⁰⁰	84(36)	0.02(1)	1.86(2)	8^{+4}_{-2}	<0.001	0	0.32(1)	1(1)	1.1(1)	0.75
17	0.34(9)	12900 ₅₂₀₀ ¹⁶⁴¹⁰⁰	100 ₂₀ ³⁰⁰	0.03(1)	1.98(1)	45(2)	<0.001	0	0.24(1)	0.64(1)	0.67(1)	0.62
18	0.34(8)	14400 ₇₂₀₀ ¹⁷³⁰⁰⁰	100 ₂₀ ³⁰⁰	0.02(1)	1.95(2)	21(2)	<0.001	0	0.20(1)	0.54(2)	0.57(1)	1.02
19	–	–	–	–	2.02(1)	28(3)	<0.001	0	0.21(1)	0.49(2)	0.51(1)	0.85
20	–	–	–	–	1.90(1)	4(2)	0.254	$0.15^{+0.85}_{-0.15}$	0.11(1)	0.32(1)	0.34(1)	0.78
21	–	–	–	–	1.91(1)	4(3)	1.0	$0^{+0.6}_{-0.15}$	0.10(1)	0.28(1)	0.31(1)	0.72
22	–	–	–	–	2.17(1)	11(3)	<0.001	0	0.17(1)	0.28(1)	0.31(1)	0.77
23	–	–	–	–	2.08(1)	1.0(1)	1.0	0	0.10(1)	0.21(1)	0.23(1)	0.40

Note. — Basic model parameters and normalizations quoted with 90% confidence limits. Model components include a multicolor blackbody, a Gaussian, and Pexriv. All fluxes are measured in the 3.5–20.0 keV band, as are all model parameters and normalizations. Where errors are not quoted, the error does not affect the value of the last significant digit. Fits to the VHS and HS have 30 *dof* when red and blue lines are fit, and 36 *dof* when lines are not fit. Fits to the LS have 33 *dof* when the blue line is fit, 36 *dof* when they are not. Quoted χ^2 values are for models including lines. All observations fit with 0.75% systematic errors added, and (fixed) $N_H = 7.5 \times 10^{22} \text{ cm}^{-2}$. R_{DBB} is the disk-blackbody-derived inner radius, calculated for a disk inclination of 45 degrees (assumed), and a distance of 8 kpc. The Pexriv power-law cut-off energy is fixed at 200 keV, and the disk inclination at 45 degrees. f is the disk reflection fraction, $0.0 < f < 1.0$ corresponds to the range $0 - 2\pi$, and F-stat is the standard F statistic, measuring the significance of f .

† denotes an observation where the ionization is fixed at 2000.

Table 3: Fe K_αLine Parameters

Obs.	Centroid Energy (keV)	Width (keV)	Eq. Width (eV)	Flux 10^{-11} cgs	χ^2/dof w/o line	χ^2/dof w/ line	F-stat.
— Red Wing —							
— Very High State —							
3	4.6(1)	$0.2^{+0.1}_{-0.2}$	76(15)	17(2)	4.19	1.02	<0.001
4	4.6(1)	0.4(1)	105(15)	22(3)	5.62	0.64	<0.001
5	4.6(3)	0.3(2)	69(14)	12(3)	2.97	0.49	<0.001
6	4.5(2)	$0.3^{+0.2}_{-0.3}$	51(14)	8(2)	1.87	0.45	<0.001
7	4.5(2)	0.3(3)	57(15)	8(2)	1.96	0.34	<0.001
8	4.7(1)	0.5(1)	96(14)	9(1)	4.62	0.50	<0.001
— High State —							
9	4.5(2)	0.3(3)	39(12)	7(2)	1.35	0.42	<0.001
10 [†]	4.5(3)	$0^{+0.5}$	23(9)	4(2)	1.00	0.69	0.14
11	4.5(2)	$0^{+0.5}$	20(9)	3(1)	0.83	0.45	0.04
12	—	—	—	—	—	—	—
13	—	—	—	—	—	—	—
13.1	—	—	—	—	—	—	—
14	—	—	—	—	—	—	—
15	—	—	—	—	—	—	—
— Blue Wing —							
— Very High State —							
3	5.8(1)	0.8(1)	120(20)	19(4)	5.42	1.02	<0.001
4	6.3(2)	0.4(2)	66(16)	10(2)	2.49	0.64	<0.001
5	6.3(3)	0.5(3)	51(19)	6(2)	1.57	0.49	<0.001
6	6.4(3)	0.5(4)	45(16)	5(2)	1.25	0.45	0.002
7	6.4(3)	0.4(4)	39(18)	4(1)	1.09	0.34	<0.001
8	6.6(2)	0.4(3)	60(18)	4(1)	2.00	0.50	<0.001
— High State —							
9	6.4(3)	$0.4^{+0.3}_{-0.4}$	39^{+19}_{-12}	4(2)	1.20	0.42	0.002
10 [†]	6.5(3)	$0.3^{+0.6}_{-0.3}$	30^{+20}_{-12}	3(1)	1.07	0.69	0.103
11	6.6(3)	$0.1^{+0.7}_{-0.1}$	29^{+15}_{-12}	2(1)	1.03	0.55	0.036
12	6.8(2)	$0.0^{+0.5}$	33(10)	3(1)	1.31	0.70	0.036
13	6.7(1)	$0.0^{+0.3}$	56^{+14}_{-11}	2(1)	2.19	0.69	<0.001
13.1	6.8(1)	0.2(2)	88^{+19}_{-16}	2.0(4)	3.13	0.45	<0.001
14	6.74(9)	0.2(2)	130(19)	2.0(3)	5.96	1.13	<0.000
15	$6.69^{+0.09}_{-0.04}$	0.2(1)	347(31)	4.8(5)	23.7	0.94	<0.001
— Low State —							
16	6.68(4)	$0.06^{+0.14}_{-0.06}$	193(13)	1.8(1)	16.9	0.75	<0.001
17	6.72(3)	0.30(5)	420(19)	2.3(1)	44.6	0.62	<0.001
18	6.71(3)	0.32(4)	508(22)	2.4(1)	50.1	1.02	<0.001
19	6.68(3)	0.20(8)	545(25)	2.3(1)	32.6	0.85	<0.001
20	6.80(3)	0.24(7)	574(30)	1.6(1)	27.0	0.78	<0.001
21	6.77(3)	0.24(6)	661(36)	1.7(1)	25.8	0.72	<0.001
22	6.65(4)	0.34^{+16}_{-12}	931(54)	2.5(1)	30.4	0.77	<0.001
23	6.78(3)	0.26(4)	967(40)	1.6(1)	30.5	0.40	<0.001

Note. — Line parameters, normalizations, and fluxes, are all quoted with 90% confidence limits. Fits to the VHS and HS have 30 *dof* when red and blue lines are fit, and 36 *dof* when lines are not fit. Fits to the LS have 33 *dof* when the blue line is fit, 36 *dof* when they are not. The *F*-statistic is the classic f-test statistic. Observations 12, 13, 13.1, 14, and 15 are not consistent with the inclusion of a red wing.

† denotes observations where measurements constrain parameters but do not meet our criterion for statistical significance.

Table 4: Three Methods to R_{in} in the VHS

Obs.	$\nu_{QPO}^{(a)}$ (Hz)	$R_{\text{in}}^{(b)}$ (R_g)	$R_{\text{in}}^{(c)}$ (R_g)	$R_{\text{in}}^{(d)}$ (R_g)
3	31.6(2)	4.38(1)	2.8(1)	1.2(1)
4	31.3(2)	4.39(1)	2.8(1)	1.3(1)
5	23.7(1)	4.84(1)	3.0(1)	1.3(1)
6	20.2(1)	5.12(1)	3.2(1)	1.4(1)
7	20.0(1)	5.14(1)	3.2(1)	1.4(1)
8	22.6(2)	4.92(1)	3.1(1)	1.2(1)

Note. — R_{in} values in R_g . In the VHS, the Laor relativistic disk line emission model can be fit to the Fe K_{α} profile with $R_{\text{in}} = 1.2 R_g$ with statistical significance comparable to that of the Gaussian model. The relation described by DiMatteo & Psaltis (1999) is shown in Equation 1 within the text. Given ν_{QPO} and assuming a BH mass, an inner disk radius may be derived assuming Keplerian orbits up to the marginally stable orbit.

- (a) QPO frequencies reported by Revnivtsev et al. 1999.
- (b) Calculated via Equation 1 for $M_{BH} = 5.0 M_{\odot}$.
- (c) Calculated via Equation 1 for $M_{BH} = 10.0 M_{\odot}$.
- (d) The multicolor blackbody disk radius.

Table 5: LS observations fit with the Diskline model

Obs.	E_{cent} (keV)	R_{in} (R_g)	EW (eV)	Flux(3–25 keV) 10^{-11} cgs	χ^2/dof (Gaussian)	χ^2/dof (diskline)
16	6.68(4)	63^{+933}_{-31}	200(12)	2.1(1)	0.75	0.55
17	6.72(3)	25^{+26}_{-19}	411(16)	2.5(1)	0.62	0.77
18	6.69(3)	6^{+15}_{-15}	533(19)	2.6(1)	1.02	0.81
19	6.70(4)	102^{+140}_{-63}	525(24)	2.6(1)	0.85	0.91
20	6.81(4)	22^{+33}_{-16}	612(29)	1.8(1)	0.78	0.89
21	6.78(3)	25^{+29}_{-19}	682(27)	1.8(1)	0.72	0.80
22	6.65(4)	14^{+12}_{-8}	915(41)	2.9(1)	0.77	0.96
23	6.79(3)	35^{+34}_{-15}	916(33)	2.0(1)	0.40	0.80

Note. — We fix R_{out} at $10^4 R_g$, the emissivity profile to r^{-2} , and the disk inclination at 45 degrees. With these parameters fixed, and using the pexriv parameters obtained via fitting with a Gaussian line model, we measure line centroid energy (E_{cent}), inner radius (R_{in}), equivalent width (EW), the 3.5–20.0 keV line flux, and the reduced χ^2 values for fits with a Gaussian, and with diskline. Errors are 90% confidence limits. Fits have 36 dof without the diskline model, 33 dof with the model. All fits with the diskline model are significant at greater than 99.9% confidence. Although the relative χ^2 values do not demand the diskline over the Gaussian model, the parameters of the diskline model are very well-constrained.

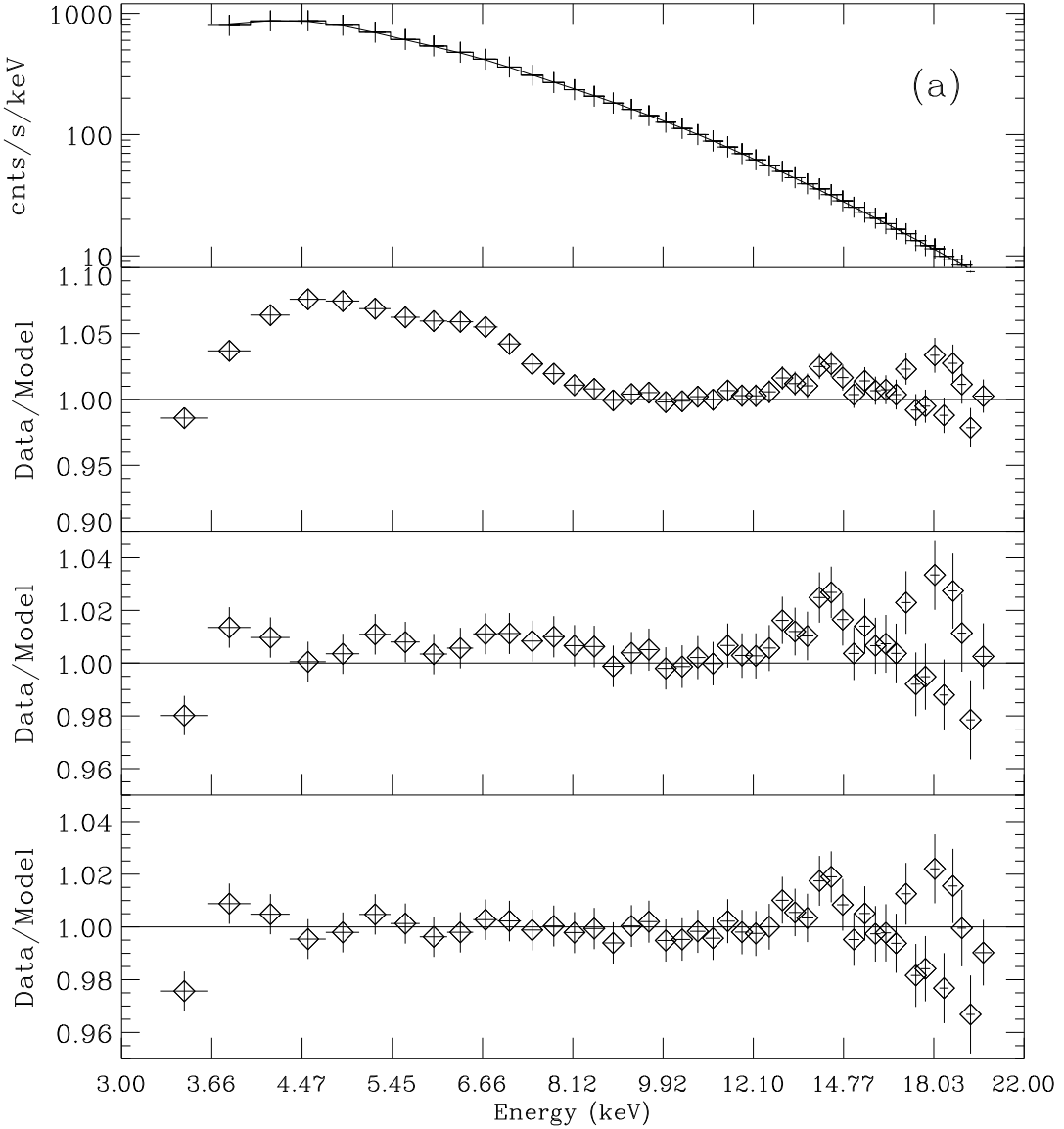
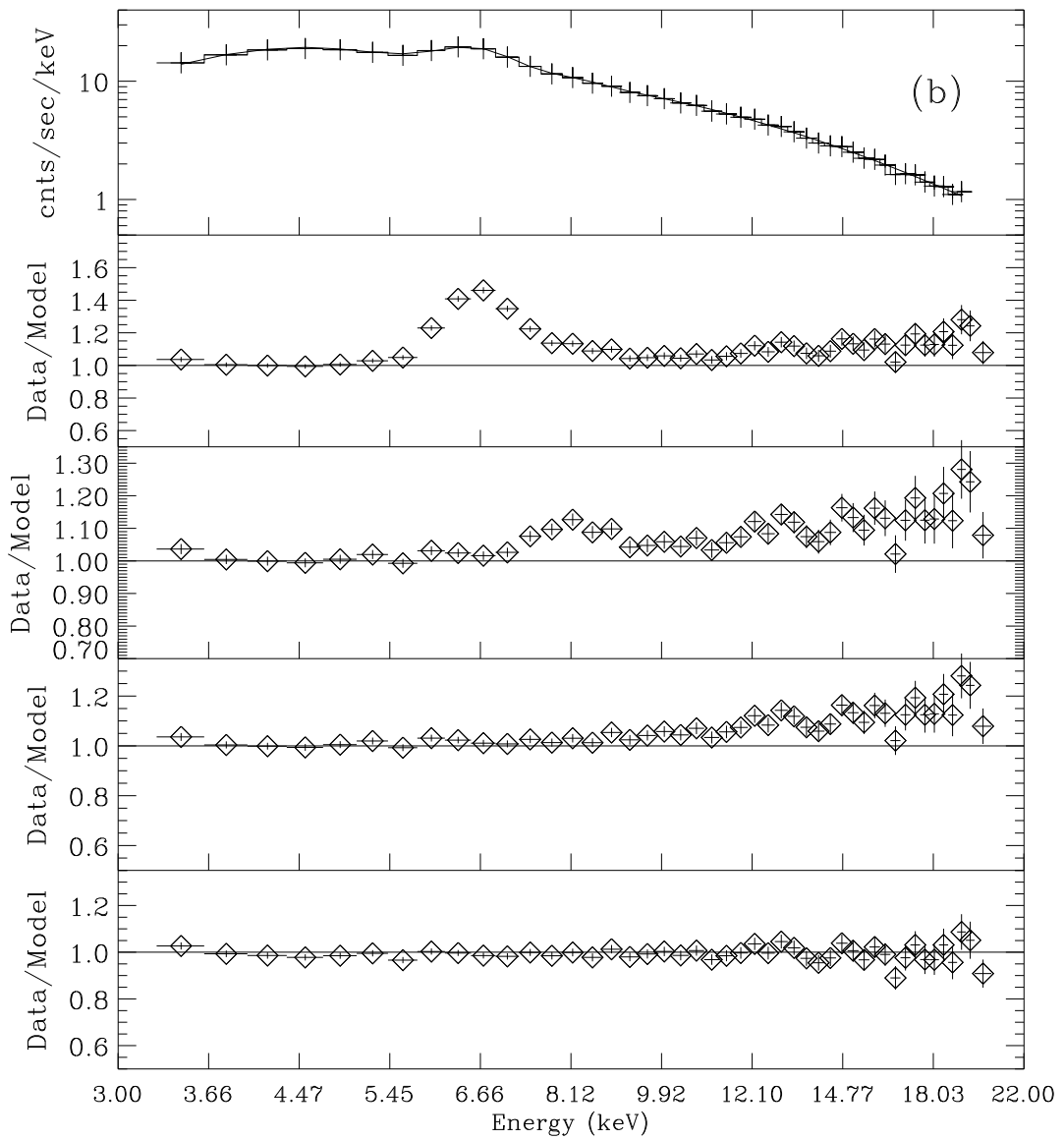


Fig. 2.— Typical spectra and data/model profiles from the VHS and LS. (a) Observation 3 (VHS). The top plot shows the spectrum for Observation 3, fit with a blackbody disk + 2 Gaussians + Pexriv model. The plots below are data/model ratio plots. Second from top, dbb + plaw; notice the double line peaks and the reflection above 10 keV. The third plot is the ratio for a model consisting of dbb + 2 Gaussians + plaw; the lines are fit well but the reflection is not. Finally, at bottom, the ratio for a model consisting of dbb + two gs + pexriv; this model fits the lines and continuum very well. (b) Observation 19 (LS). The top plot shows the spectrum for Observation 19, fit with a 2 Gaussians plus Pexriv model. The plots below are data/model ratio plots. Second from top, p-law; notice the very strong, broadened line and reflection. The third plot is the ratio for a model consisting of a Gaussian + plaw; the lines is fit well, but a higher energy line remains. Fourth, the ratio for a model with 2 g's + plaw; this is a good fit. At bottom, the ratio for a model consisting of two g's + reflection via pexriv.



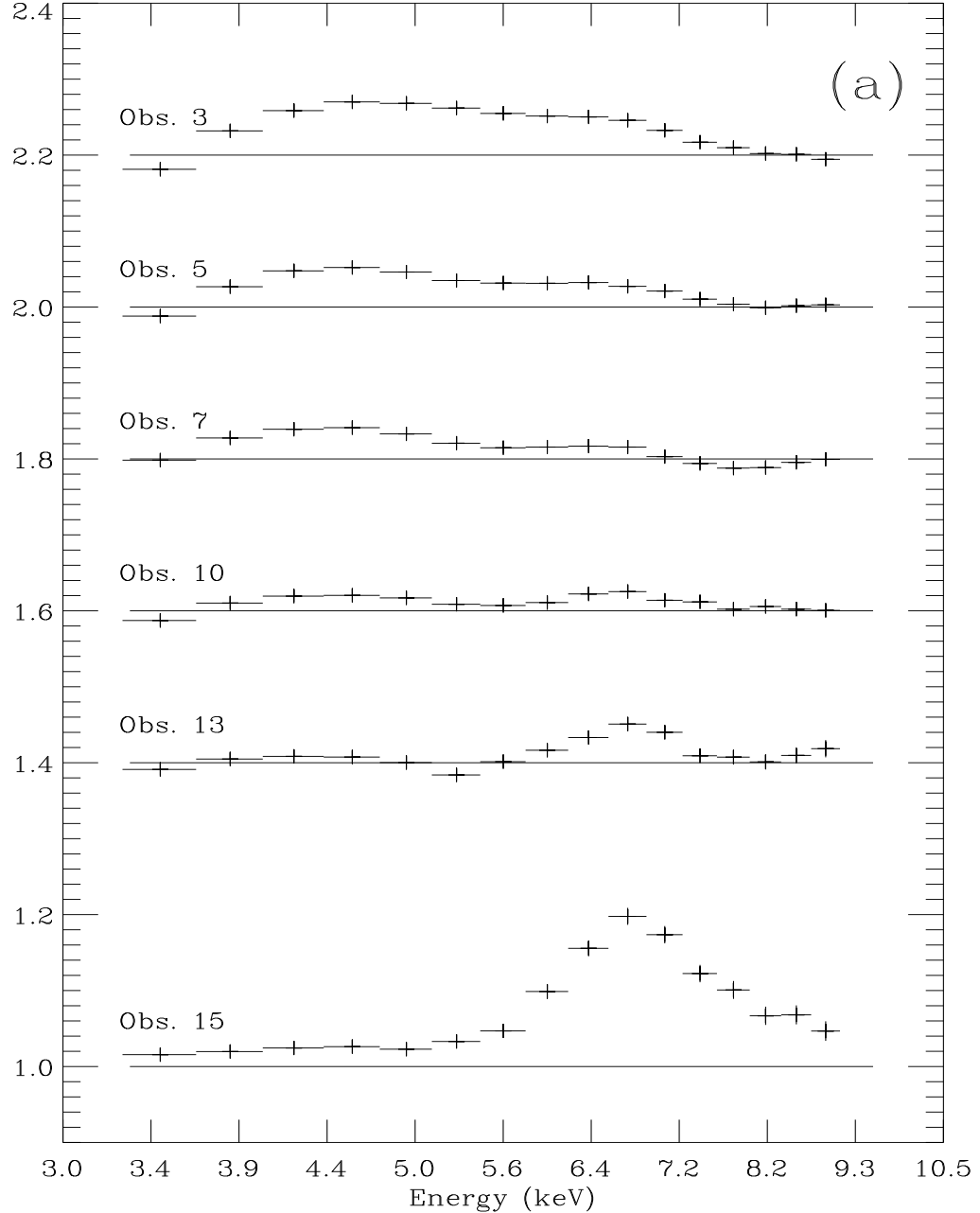
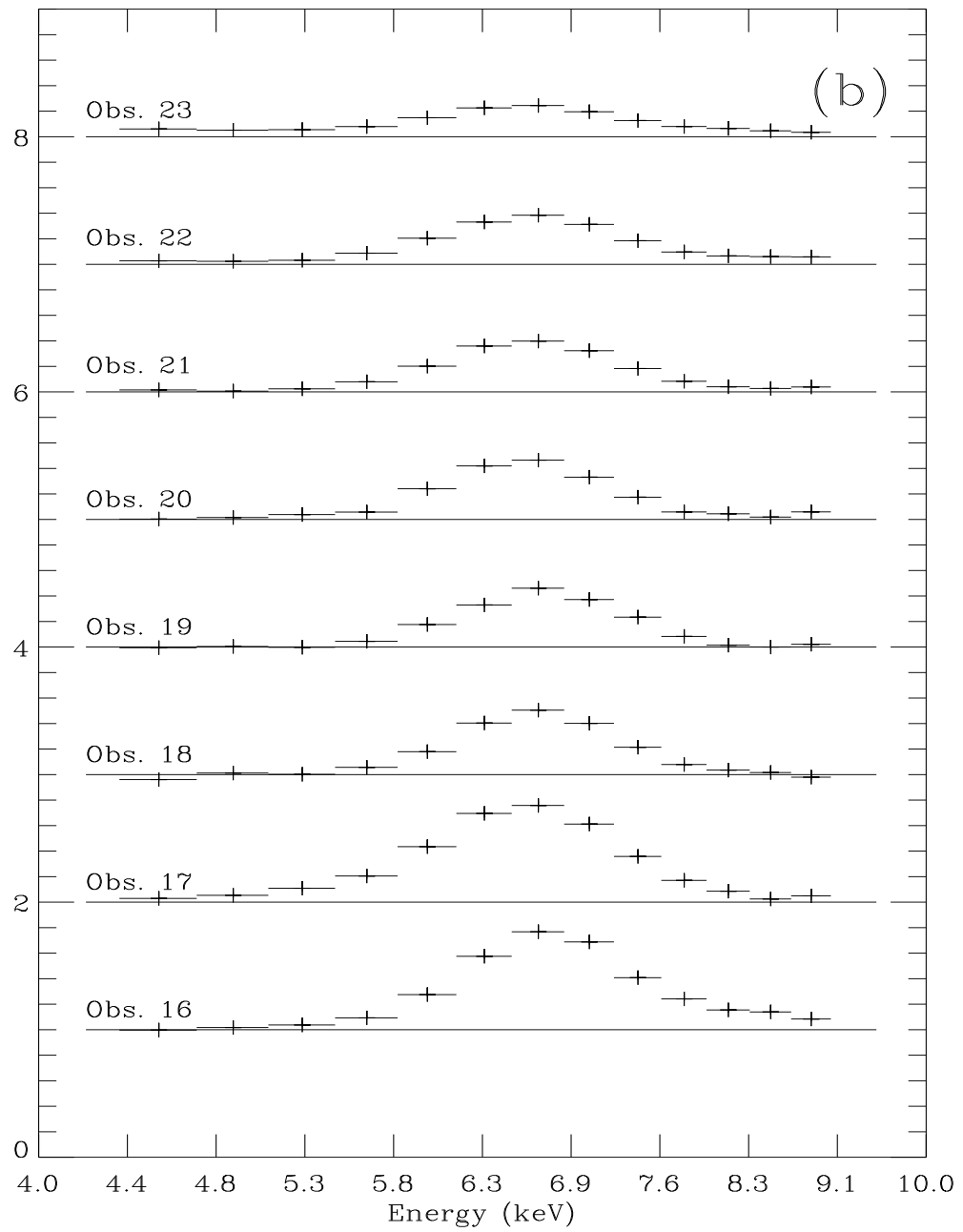


Fig. 3.— Data/model ratios across the outburst. (a) VHS and HS: Models include only the basic multicolor blackbody disk plus power-law components. Observations are offset with respect to each other for clarity; however, the absolute scale is the same for all. The emission excess in observation 3 (at top) is double-peaked, but by the middle of the HS it is clear the profile is becoming single-peaked. Finally, in observation 15 (at bottom) the line feature is very strong and broad. (b) LS: The model is the basic power-law only. It is clear that the line is very prominent relative to the continuum in the LS. Some variation in line centroid energies and widths can be discerned.



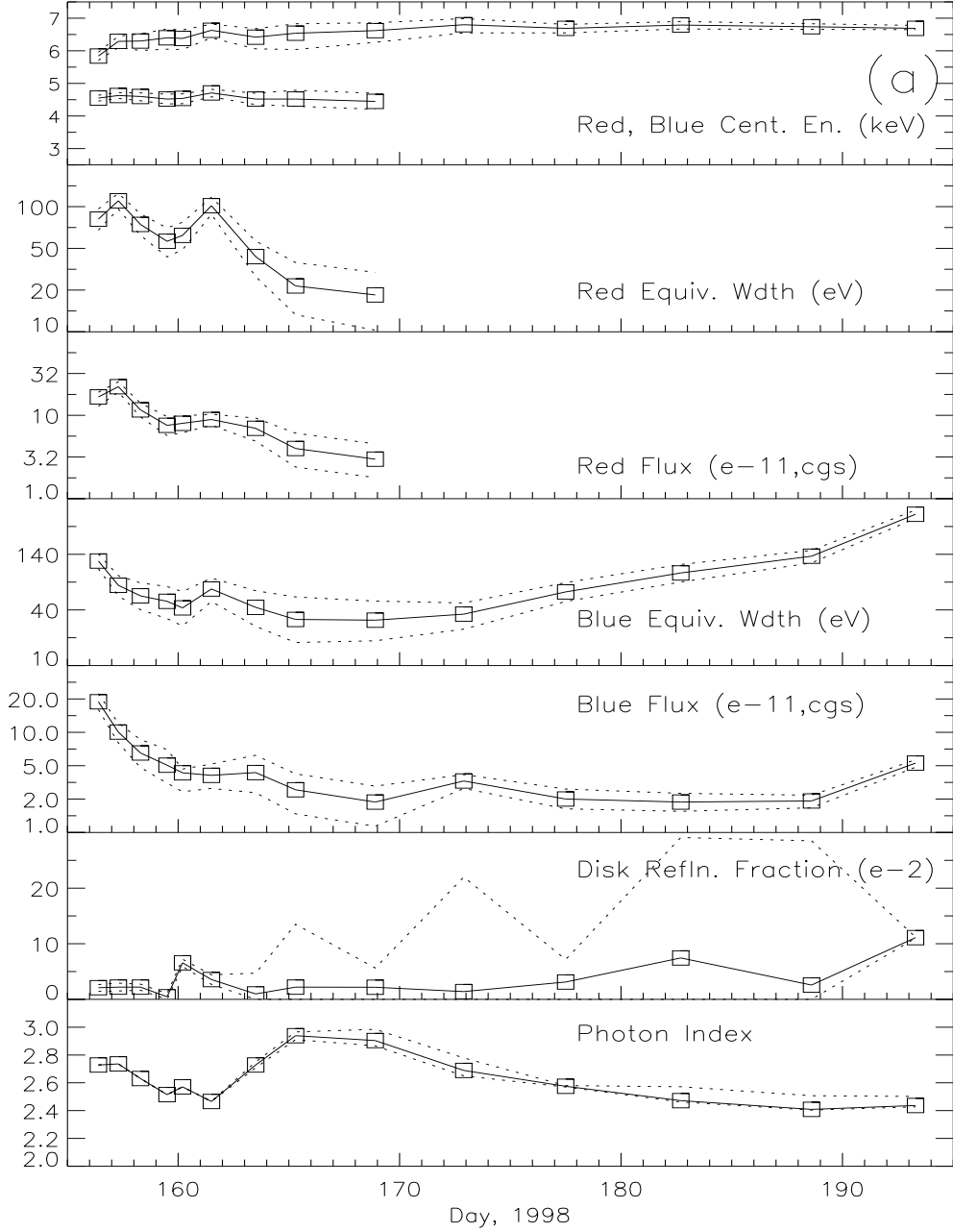


Fig. 4.— Line and Reflection Parameters. Measured values are connected by a continuous line, and 90% confidence limits by dotted lines. (a) VHS and HS. Top to bottom: red and blue wing centroid energy (top); red wing equivalent width; red wing flux; blue line equivalent width; blue wing flux; disk reflection fraction; and power-law photon index (bottom); vs Day of Outburst (days from 3.8 June 1998). The disk ionization parameter is high throughout the VHS and HS; $\xi \geq 2.0 \times 10^3$. (b) LS. Top to bottom: Fe K α centroid energy (top); Fe K α equivalent width; Fe K α flux; disk reflection fraction; and power-law photon index (bottom); vs Day of Outburst. The disk ionization parameter is low in the LS; $0 \leq \xi \leq 100$.

